acterize primitive anthropoids. There are also other possible Asian claimants to higher primate status, such as *Pondaungia*, *Hoanghonius*, or *Amphipithecus* (*19*), for which, unlike *Eosimias*, ranking in Anthropoidea might be a possibility. Paleogene faunas and floras show that some sort of interconnection existed then between northeast Africa and southern Asia, and thus, this suborder could have reached both regions in the Eocene. Nevertheless, neither *Hoanghonius* nor the Burmese Eocene fossils preserve the skull and front teeth, which, if they existed and were like those of Anthropoidea, would make their ordinal or subordinal ranking certain. Even if the Burmese forms were to prove to be definite anthropoideans, they could just as well be outmigrants from Africa as from anywhere else.

Fayum mammals also indicate that there was faunal interchange with Europe, but Europe lacks evidence of early anthropoideans. Recent discoveries at Glib Zegdou in Algeria described as *Algeripithecus* (*20*), *Tabelia* (*21*), and a form called *Djebelemur* from Chambi, Tunisia (*22*), are all forms that resemble in various ways the Fayum L-41 primates but are earlier in age. There is some evidence that the Algerian and Tunisian forms either are primitive anthropoideans or, in the case of the mandible of *Djebelemur*, relate to the cercamoniine group. Together, these latter primates and those from L-41 appear to root the earliest higher primates in the cercamoniine radiation. There have often been differences in deciding whether *Oligopithecus*, *Hoanghonius*, or *Algeripithecus* should be ranked as adapoids or as anthropoids (*6*, *8*, *21*). This is because of the high degree of similarity in the cheek tooth crowns of both groups, especially now that we understand the L-41 anthropoideans so fully. Thus, these shared-derived features do not involve just the front teeth but the entire dentition. The approximation of these two groups, which makes their molars difficult to tell apart, extends also to time and place, because a cercamoniine has been found at L-41 (*6*). The foregoing conclusions bring into question the existence of an haplorhine clade. The best evidence is that the origin of Anthropoidea was in Africa. Anthropoids either arose from a cercamoniine-like ancestor or from a similar endemic African group.

REFERENCES AND NOTES

1. H. F. Osborn, *Bull. Am. Mus. Nat. Hist.* **24**, 265 (1908); M. Schlosser, *Beitr. Paläontol. Geol. Öst.-Ung.* **24**, 51 (1911); J. J. Kälin, *Ann. Paleontol.* **47**, 1 (1961); E. L. Simons, *Nature* **205**, 135 (1965); R. F. Kay, J. G. Fleagle, E. L. Simons, *Am. J. Phys. Anthropol.* **55**, 293 (1981); E. L. Simons, *J. Hum. Evol.* **16**, 273 (1987).
2. E. L. Simons, *Proc. Natl. Acad. Sci. U.S.A.* **86**, 9956 (1989).
3. ———, *ibid.* **89**, 10743 (1992).
4. ———, *Science* **247**, 1567 (1990); ———, D. T. Rasmussen, T. M. Bown, P. S. Chatrath, in *Anthropoid Origins*, J. G. Fleagle and R. F. Kay, Eds. (Plenum, New York, 1994), pp.179–202; D. T. Rasmussen and E. L. Simons, *Int. J. Primatol.* **13**, 477 (1992).
5. E. L. Simons and D. T. Rasmussen, *Proc. Natl. Acad. Sci. U.S.A.* **91**, 9946 (1994).
6. ———, P. D. Gingerich, *J. Hum. Evol.*, in press.
7. A. Walker, in *Calibration of Hominoid Evolution*, W. W. Bishop and J. A. Miller, Eds. (Scottish Academic Press, Edinburgh, 1972), p. 195.
8. P. D. Gingerich, *Geobios Mem. Spec.* **1**, 165 (1977).
9. ———, *J. Hum. Evol.* **10**, 345 (1981).
10. A. L. Rosenberger, E. Strasser, E. Delson, *Folia Primatol.* **44**, 15 (1985).
11. J. L. Franzen, in *Anthropoid Origins*, J. G. Fleagle and R. F. Kay, Eds. (Plenum, New York, 1994), pp. 99–122.
12. A. L. Rosenberger and F. S. Szalay, in *Evolutionary Biology of the New World Monkeys and Continental Drift*, R. L. Ciochon and A. B. Chiarelli, Eds. (Plenum, New York, 1980), pp. 139–158.
13. P. D. Gingerich, *Am. J. Phys. Anthropol.* **56**, 217 (1981).
14. L. Krishtalka, R. K. Stucky, K. C. Beard, *Proc. Natl. Acad. Sci. U.S.A.* **87**, 5223 (1990).
15. W. B. Spatz, *Folia Primatol.* **9**, 22 (1968).
16. E. L. Simons and D. T. Rasmussen, *Am. J. Phys. Anthropol.* **79**, 1 (1989).
17. B. Sige, J.-J. Jaeger, J. Sudre, M. Vianey-Liaud, *Palaeontographica* **214**, 31 (1990). Paleocene *Altiatlasius* from Morocco, on the basis of composite arrangements of unassociated and referred isolated teeth only, was said to be an omomyid primate that should be ranked as the sister group of the Anthropoidea; a later study (*23*) has cast doubt on whether *Altiatlasius* is even a true primate rather than a proprimate, and it shows no derived omomyid features.
18. K. C. Beard, T. Qi, M. R. Dawson, B. Wang, C. Li, *Nature* **368**, 604 (1994). These authors explicitly state that there are six unambiguous characteristics that place *Eosimias* in the Anthropoidea. In fact, the six derived features they give can all be found in both modern and Eocene prosimians, and thus, none of them justify assignment to Anthropoidea. This is not to say that early anthropoids could not have been in Asia, but more and better evidence is needed.
19. B. Maw, R. L. Ciochon, D. E. Savage, *Nature* **282**, 65 (1979); R. L. Ciochon and P. Holroyd, in *Anthropoid Origins*, J. G. Fleagle and R. F. Kay, Eds. (Plenum, New York, 1994), pp.143–162.
20. M. Godinot and M. Mahboubi, *Nature* **357**, 324 (1992).
21. M. Godinot, in *Anthropoid Origins*, J. G. Fleagle and R. F. Kay, Eds. (Plenum, New York, 1994), pp. 235–295.
22. J.-L. Hartenberger and B. Marandat, *Hum. Evol.* **7**, 9 (1992).
23. P. D. Gingerich, *Nature* **346**, 411 (1990).
24. Illustrations were prepared by R. L. Usery. This is Duke Primate Center publication 597. My thanks go to the National Science Foundation and staff of the Egyptian Geological Survey for support of the research and to D. T. Rasmussen, F. C. Howell, I. M. Tattersall, T. M. Bown, F. A. Ankel-Simons, and P. D. Gingerich for reviewing the manuscript.

12 December 1994; accepted 25 April 1995

A Scattered-Wave Image of Subduction Beneath the Transverse Ranges

J. Revenaugh

Over 5600 short-period recordings of teleseismic events were used to create deterministic maps of *P*-wave scatterers in the upper mantle beneath Southern California. Between depths of 50 and 200 kilometers, the southern flank of the slab subducting beneath the Transverse Ranges is marked by strong scattering. The marked scattering indicates that the edge of the slab is a sharp thermal boundary. Such a boundary could be produced by slab shearing or small-scale convection in the surrounding mantle. The northern limb of the slab is not a strong scatterer, consistent with thicker lithosphere north of the Transverse Ranges.

The Transverse Ranges comprise a distinct physiographic province that cuts across the dominant, north by northwest, tectonic fabric of Southern California and showcases some of the most spectacular topography in North America. The mantle beneath the ranges, home of a 60-km-wide tabular velocity anomaly to depths in excess of 200 km (*1*, *2*), is no less spectacular. This curtain of high *P*-wave velocity draped from the Transverse Ranges is commonly believed to be subducted subcrustal lithosphere resulting from $\geq 5 \times 10^6$ years of oblique convergence across the San Andreas fault zone (*3*, *4*), but the details of the anomaly are unclear. For instance, is subduction one-sided or two-sided (*3–5*)? Does the anomaly extend from the base of the crust, or does it only appear at greater depths (*2*, *6*)? And where does the slab detach from the crust? The subhorizontal crustal detachments beneath Los Angeles and the Ventura Basin—poorly understood but capable of great earthquakes (*7*)—are tied to deeper detachments of the Transverse Ranges.

In this study, I present a mode of imaging crust and upper mantle structure that uses singly scattered energy within the coda of teleseismic *P*. The method, known as Kirchhoff coda migration (KCM) (*8*), allows imaging of short length scale ($\leq$2 km) velocity and density heterogeneity and structures transparent to travel-time tomography. The scattered-wave images are not as intuitive as tomography's, but the combination of the two methods is powerful. I applied KCM to 13 years of teleseismic seismicity recorded by the Southern California

Earth Sciences–Crustal Imaging Laboratory, University of California, Santa Cruz, CA 95064, USA.

Seismograph Network (SCSN) to map loci of significant scatterers at depths between 50 and 200 km. The results confirm intracontinental subduction and point out asymmetry in lithospheric structure across the Transverse Ranges.

In KCM, the subsurface is treated as a collection of closely spaced, isotropic point scatterers, and travel times of scattered energy are computed such that each subsurface point is mapped to time in the coda (8). The sum, correctly normalized, of data along the arrival-time surface of a scatterer measures the scatterer's strength (Fig. 1).

To implement this, let $u_{ij}(t_k)$ represent the time series recorded by the jth of M stations for the ith of N sources. Time, t_k, is referenced to a canonical start time t_0, such that $t_k = t_0 + k\Delta t$ for digitization rate $(\Delta t)^{-1}$. Energy from a source at position $\mathbf{s}_i$ scattered at position $\mathbf{x}$ and recorded at station j at position $\mathbf{r}_j$ arrives at time

$$\tau_{ij}(\mathbf{x}) = t_0 + T(\mathbf{s}_i,\mathbf{x}) + T(\mathbf{x},\mathbf{r}_j) - T(\mathbf{s}_i,\mathbf{r}_j) \quad (1)$$

on the aligned seismogram (9), where $T(\mathbf{a},\mathbf{b})$ is the travel time between points $\mathbf{a}$ and $\mathbf{b}$ (10). The migration value at $\mathbf{x}$, $S(\mathbf{x})$, is obtained from

$$S^n(\mathbf{x}) = \frac{1}{K(\mathbf{x})} \sum_{i=1}^{N} \sum_{j=1}^{M} \sum_{k=1}^{k_{max}} \{X_j(\mathbf{x})$$

$$W[\tau_{ij}(\mathbf{x}),T(\mathbf{x},\mathbf{r}_j)] \sum_{\ell} |u_{ij}(t_k - \ell\Delta t)|\}^{1/n} \quad (2)$$

Here, k_{max} is the number of recorded samples beyond t_0; $W[\tau_{ij}(\mathbf{x}),T(\mathbf{x},\mathbf{r}_j)]$ and $X_j(\mathbf{x})$ are windowing operators over time and distance, respectively, that include corrections for geometric spreading, obliquity, and receiver terms and terminate summation before arrival of secondary phases such as *PcP* and *pP*; and $K(\mathbf{x})$ is a normalizing factor numerically equal to the sum of all weights applied to data. Summation over ℓ allows for a short (0.2 to 0.5 s) running mean of data. The exponent n implements Nth-root stacking (11).

In Eq. 2, data along scatterer time surfaces are summed for many different receivers and sources, such that likely sources of scattered energy are identified by large $S(\mathbf{x})$. The size of $S(\mathbf{x})$ required to be significantly above background levels is obtained by replacing $S(\mathbf{x})$ with its cumulative probability of occurrence in noise-only data, obtained from repeated migration of trace sets with randomized station associations resulting in a bootstrap approximation of $S(\mathbf{x})$ probability density in the absence of coherent, singly scattered energy (12). Assigning seismograms to stations at random destroys the correlation structure of data without affecting amplitude/distance ratios or geographic variation in station density and source-station geometry; thus, site and geometrical effects are accounted for that would otherwise severely bias estimation (13).

The data set consists of short-period, vertical component recordings of 120 teleseismic events of intermediate and deep circum-Pacific earthquakes between 1981 and 1993. Records were obtained from 232 stations with an average of 47 stations per event. In total, 5606 seismograms were input to migration. A minimum of 500 contributing seismograms at each grid point was imposed, and migration was not performed for regions outside the SCSN with poor azimuthal station coverage. Variations in detector efficiency across the SCSN raise and lower the detection threshold such that some strong scatterers may be missed in regions of poor detection whereas globally weaker, but locally strong, scatterers in other areas are detected (Fig. 2). For the most part, variations of $S(\mathbf{x})$ about the bootstrap mean closely mimic scatterer significance such that high significance usually implies high scattering strength. To avoid confusion, however, I refer to scatterer significance as potential, such that high potential implies highly probable detection of scattered energy. Synthetic tests are used to help distinguish detector efficiency from scatterer strength and to identify experimental artifacts.

The images show that at a depth from 75 km to at least 150 km (Fig. 2, B, C, and D), a single feature dominates the scattering field: a nearly east-west–trending ridge of high potential centered on 34°N and strongest between 119° and 116°W (14). The ridge correlates well with the southern limb of the tabular velocity anomaly imaged beneath the central and eastern Transverse Ranges in a number of tomographic studies (1, 2). Although I performed migration to depths of 400 km, resolution is poor below 200 km, and it is difficult to assign a maximum depth to the ridge, although there is some evidence of a signature to 250 km. Between 75 and 200 km (Fig. 2, B through E), where resolution is best, prominent along-strike variations in potential appear to be relatively consistent with depth. I attribute some of this consistency to vertical leakage of energy during KCM, but synthetic tests suggest that significant leakage does not exceed 25 km at these depths, and I regard the vertical continuity of potential highs and lows as genuine. The ridge also appears to shift slightly to the north as depth increases, suggesting a nearly vertical northward dip, although this interpretation is debatable given the diffuse quality of the image. I refer to this feature as the 34°N high.

An equivalent northern limb to the Transverse Ranges anomaly is not seen, although there are hints of coherent patterns in the 50- to 100-km images near 35.25°N on the western edge of the study area. Synthetic tests (Fig. 3) show that a second ridge displaced 0.5° to 1.5°N, but otherwise similar to the 34°N high, would be imaged. Clearly, any northern parallel to the 34°N high is weak in comparison.

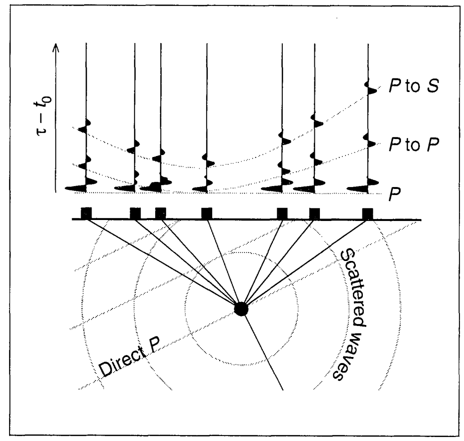

Fig. 1. Schematic illustration of the wave field from a point scatterer at depth. With seismograms aligned on *P*, secondary arrivals from the scatterer move out across the array asymmetrically as a result of the finite ray parameter of direct *P*. Scatterer strength is estimated by summing data along the *P* to *P* (or *P* to *S*) scattered-wave travel time curve with corrections for propagation effects and wavefront obliquity at the free surface. Modified bootstrap estimation is used to assign significance levels to scatterer detection.

The diffuse zone of potential highs north of 35.5°N in the southern Sierra Nevada (~118.5°W) at a depth of 50 to 100 km (Fig. 2, A, B, and C) may be related to the Lake Isabella anomaly, a 3 to 5% high velocity patch in the uppermost mantle (2, 15). Above 100 km there is intriguing visual correlation between potential highs and high gradient zones in independently obtained velocity tomograms, but potential fades rapidly below 100 km whereas the tomographic anomaly extends to ~200 km. This discrepancy has implications for the 34°N high.

The basic structural elements in the uppermost mantle beneath Southern California are well defined by tomographic maps of *P*-wave velocity; the scattered-wave images add detail to this structural picture and raise two related questions: (i) How does the near-vertical, slab-like Transverse Ranges velocity anomaly scatter teleseismic *P* waves? (ii) Why is the scattering asymmetric, that is, why is the northern limb of the anomaly not seen?

Humphreys and Hager (4) modeled the Transverse Ranges velocity anomaly as the paired subcrustal lithospheres of North America and the Pacific subducting vertically to 250 km beneath the eastern Transverse Ranges, shallowing to 100 km on the western margin. The 3.5% velocity perturbation associated with the anomaly implies a slab ~60 km wide having temperatures 400° to 550°C colder than the surrounding mantle. Scattering along the southern limb of the anomaly requires that the length scale of velocity variation, a, is much less than the seismic wavelength $\lambda = 2\pi/k$ (*16*). The wavelength of incoming teleseismic P waves ranges from about 3 to 15 km with peak energy near 8 km, implying scatterer length scales certainly less than 10 km and likely less than 5 km. A 60-km-wide slab initially 750°C cooler than the surrounding mantle, allowed to cool for 2×10^6 years (*17*), would have horizontal temperature gradients about 10° to 20°C/km, resulting in velocity gradients of 0.1 to 0.2% per kilometer. Thus, the most favorable combination of scattering sampling length and velocity gradient results in a velocity perturbation of 2%, but 0.5% is more realistic. A velocity perturbation of 2% is sufficient if the geom-

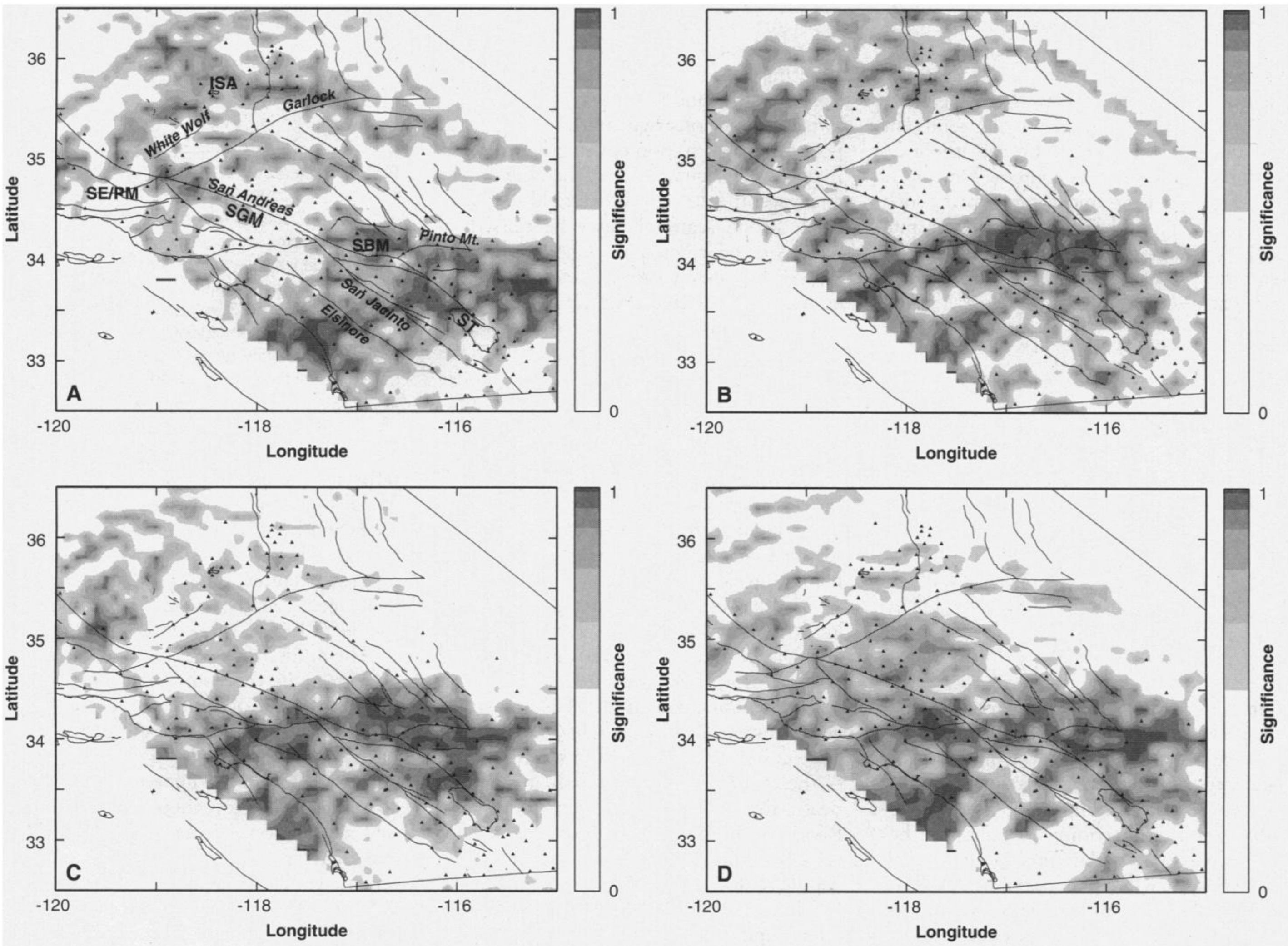

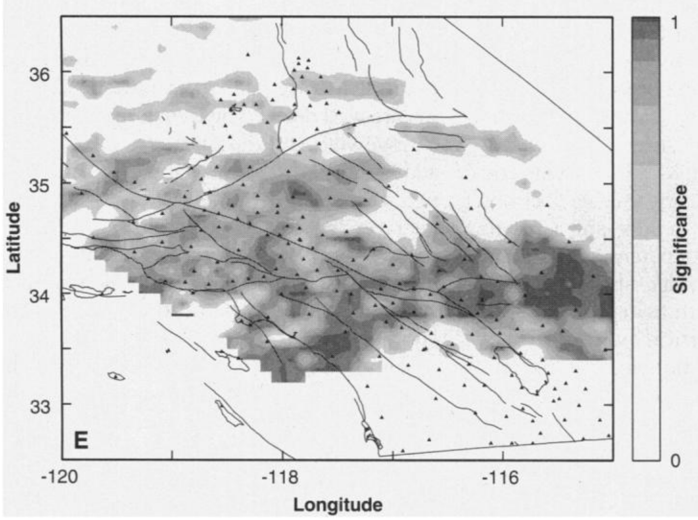

Fig. 2. (**A**) Depth slice at 50 km of the KCM for Southern California. Shown are contours of P to P scattering significance resolved on a rectangular grid with 0.1° node spacing. Values near unity imply highly significant detection of scattered energy. Solid triangles mark stations of the SCSN (additional stations outside the plot bounds were used). Because of insufficient data or poor azimuthal station coverage, no estimates were made in nonshaded regions. The Transverse Ranges are composed of the San Emigdio-Pine Mountain (SE/PM), San Gabriel (SGM), and San Bernardino (SBM) segments. ISA marks the Lake Isabella mantle anomaly; ST marks the Salton Trough. (**B**) Depth slice at 75 km. Note the distinct high-potential ridge along 34°N. (**C**) Depth slice at 100 km. (**D**) Depth slice at 150 km. (**E**) Depth slice at 200 km. Because of decreased resolving power, only grid points sampled by ≥2500 seismograms are shown in (D).

etry of heterogeneity favors scattering and energy is scattered more or less isotropically over the 70° range of scattering angles sampled, but neither of these conditions is easily reconciled with a near-vertical, tabular thermal anomaly—a poor scatterer of near-vertical *P* waves whose smooth horizontal velocity gradients favor coherent reflection (directionally dependent radiation) over aziumthally isotropic scattering.

Additional insight into the scattering strength of downwelling mantle can be gleaned from the absence of the Lake Isabella scattering signature below 100 km. Jones *et al.* (*15*) attributed the tomographic anomaly to downwelling in the mantle. Above 100 km where the thermal contrasts have had little time to diffuse and remain sharp, the anomaly is apparent in the scattering image, but at greater depths the increasingly broad diffusive boundaries lose their scattering signature despite having greater overall velocity contrast. The Transverse Ranges anomaly ought to behave similarly.

The inadequacy of simple slab geometry and the vertical continuity of high-potential sites along the 34°N high suggest an alternative: scattering from slab corners produced by simple shear during oblique subduction. I favor a shearing mechanism, as depicted in Fig. 4: It not only produces corners that radiate energy out in all directions, but it also enhances the contrast in temperatures by exposing cooler (core) lithosphere to the surrounding mantle. Corners produced by shear may correspond to the high-potential patches at 75 to 150 km in the *P* to *P* migration images (*18*). The block-like character of the Transverse Ranges anomaly in the tomographic studies is consistent with the notion of pervasive shear planes, and there is some correspondence between the block edges and the loci of high scattering potential along the southern limb of the anomaly. The prominent breaks in along-strike geometry of the Transverse Ranges at the junctures of the western San Emigdio–Pine Mountain, central San Gabriel, and eastern San Bernardino segments might be mirrored in breaks in the down-going slab. Diffusive erosion of thermal anomalies at shear corners ultimately destroys the scattering signal (*19*). Slow clockwise rotation of the San Andreas fault in the Big Bend region (*3*), if it is occurring, might maintain scattering at depth by increasing slab shear during subduction.

Scattering from shear corners, as part of the deformation mandated by oblique subduction (*4*), appears capable of accounting for the 34°N high. It does not, however, account for the absence of scattering from the northern limb of the Transverse Ranges anomaly, which I propose is due to subduction of less active (that is, more thermally mature) lithosphere north of the Transverse Ranges, reducing the temperature contrast along shear planes and slab corners. There are alternatives to this scenario. (i) Subduction is itself asymmetric (one-sided), producing high-temperature gradients where cool lithosphere recently at the base of the crust comes into direct contact with the mantle. A south-over-north geometry correctly locates scattering along the southern edge of the tomographic anomaly but conflicts with the slight northward dip of the 34°N high and the symmetry of the tomographic anomaly viewed perpendicular to the Transverse Ranges (*2*). One-sided subduction also requires that the Pacific lithosphere move around, rather than through, the Big Bend region, which seems implausible. (ii) If the proposed mechanism for the 34°N high is correct, asymmetric scattering would result if North American lithosphere is converging perpendicular to the Transverse Ranges and no shear during subduction is required. I do not favor this case because, north of the Garlock fault, the San Andreas fault system trends at roughly a 45° angle to the Transverse Ranges, suggesting oblique convergence north of the Transverse Ranges as well. (iii) The large lateral temperature contrasts associated with pervasive shear as illustrated in Fig. 4 would superpose small-scale structure on regional convective flow. Although this would hasten dispersal of the thermal anomaly (and hence the scatterer), it could augment scattering strength along portions of the slab's southern limb, with absence of a northern high-potential ridge attributed to lower temperatures (and higher viscosity) resulting in laminar flow. Whether small-scale convective flow is a strong source of scattering or is responsible for the marked north-south asymmetry is difficult to say, but it is a potential contributor to the 34°N high.

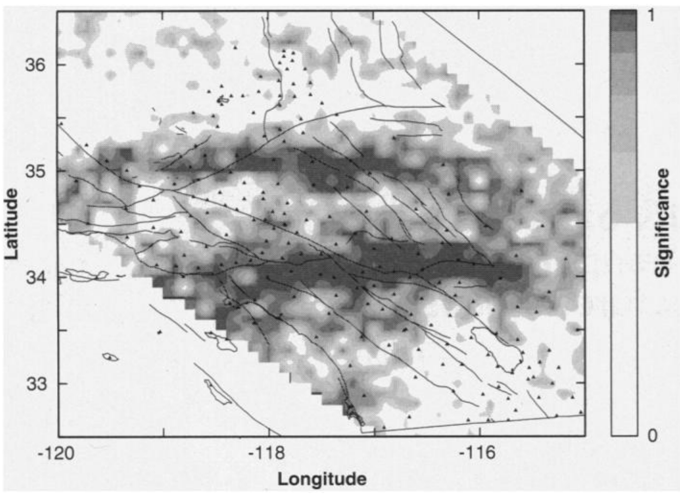

Fig. 3. Depth slice at 100 km of a synthetic experiment with two planes of isotropic scatterers aligned along 34° and 35°N between 119° and 116°W (the northern plane is shifted 0.5°W). Scatterers are placed at 0.5° along the strike and every 25 km down-dip (80°) at depths between 50 and 150 km. The synthetic data replicate experimental geometry and include high noise levels, strong signal attenuation, and ±1-s travel time variations. The northern plane is well imaged, demonstrating that the experimental geometry is favorable for detection of a northern limb to the Transverse Ranges anomaly.

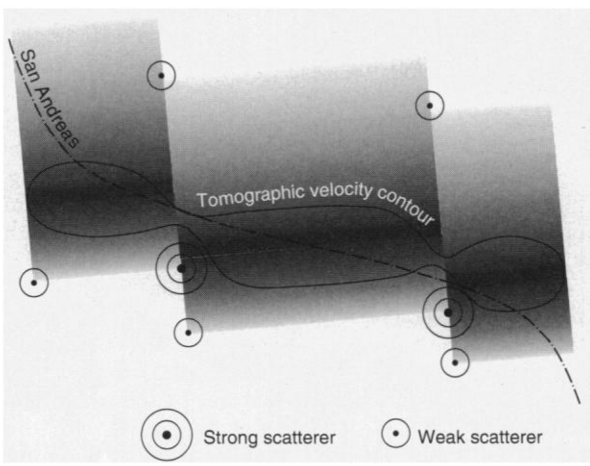

Fig. 4. Schematic depth slice of the Transverse Ranges slab illustrating the relation of slab shear and strong scattering sites. Shear is mandated by oblique subduction (*4*), although the prominent corners may derive from along-strike breaks in the deformation front along the Transverse Ranges. Shading refers to velocity, with dark areas being fast; also shown is a velocity contour spatially averaged as in tomography. Thicker lithosphere and lower thermal gradients north of the slab axis reduce scattering strength at shear corners, which accounts for the absence of a northern scattering high.

REFERENCES AND NOTES

1. S. A. Raikes, *Geophys J. R. Astron. Soc.* **63**, 187 (1980); G. Hu, W. Menke, C. Powell, *J. Geophys. Res.* **99**, 15245 (1994).

2. E. D. Humphreys and R. W. Clayton, *J. Geophys. Res.* **95**, 19725 (1990).
3. P. Bird and R. W. Rosenstock, *Geol. Soc. Am. Bull.* **95**, 946 (1984).
4. E. D. Humphreys and B. H. Hager, *J. Geophys. Res.* **95**, 19747 (1990).
5. B. Sheffels and M. McNutt, *ibid.* **91**, 6419 (1986).
6. D. Hadley and H. Kanamori, *Geol. Soc. Am. Bull.* **88**, 1469 (1977).
7. R. S. Yeats, *J. Geophys. Res.* **88**, 569 (1983); E. Hauksson and L. M. Hones, *ibid.* **94**, 9569 (1989); T. L. Davis, J. Namson, R. F. Yerkes, *ibid.*, p. 9644.
8. J. Revenaugh, *Geophys. Res. Lett.* **22**, 543 (1995).
9. First arrivals (teleseismic *P* waves) of all records are aligned on t_0. This eliminates delays accrued before entry into the study area and from shallow structure beneath stations.
10. Travel times are based on the IASP91 model of B. L. N. Kennett, in *International Association of Seismology and Physics of the Earth's Interior (IASPEI) 1991 Seismological Tables*, B. L. N. Kennett, Ed. (Research School of Earth Sciences, Australian National University, Canberra, 1991). Velocity heterogeneity dephases scattered energy, resulting in lowered stack amplitudes; the use of unsigned data and running means partially alleviates phase incoherence but reduces resolution.
11. *N*th-root stacking is discussed in P. L. McFadden, B. J. Drummond, S. Kravis, *Geophysics* **51**, 1879 (1986). Linear stacking has $n = 1$; higher values of n result in better suppression of incoherent energy. I use sixth-root stacking ($n = 6$), but results are stable for $1 \leq n \leq 8$.
12. This is not a true bootstrap, which would approximate the distribution of observed $S(\mathbf{x})$; although that is not without interest, I am most concerned with the significance of scatterer detection that necessitates estimation of the distribution of $S(\mathbf{x})$ in the absence of scattered energy. At each migration point 1000 bootstrap iterations were performed.
13. Finite source duration and source-side scattering are treated by deconvolution of a generalized source-time function obtained from a linear stack of all stations that recorded the event. The bootstrap includes station-side reverberations due to coherent crustal reflections and basin resonances, minimizing their effects on scattering potential.
14. Synthetic tests of linear arrays of point scatterers at these depths reveal a tendency of KCM to extend scattering beyond its true spatial terminus and to warp the ends down or up depending on location within the SCSN, explaining the "frowns" outside the range 119° to 116°W. See Fig. 3.
15. C. H. Jones, H. Kanamori, S. W. Roecker, *J. Geophys. Res.* **99**, 4567 (1994).
16. This conclusion is reached on the combined basis of: (i) success of the isotropic scattering model (highly directional or very low-angle scattering would be strongly damped); (ii) consistency of results over a range of scattering angles; and (iii) temporal localization of energy on the seismogram (Eq. 2 sums less than 1 s of data per seismogram per scatterer), all of which are consistent with $ka \ll 1$; K. Aki and P. G. Richards, *Quantitative Seismology* (Freeman, San Francisco, 1980).
17. A period of 2×10^6 years is less than half the duration of subduction (*4*); thus, the predicted width of the boundary layer is a lower bound favoring scattering.
18. Scattering from planar contacts within the slab also occurs but is minor because the radiation pattern is highly directional.
19. Although it is not possible to directly estimate absolute scattering strength from nonlinear stacks, forward modeling suggests that slab-induced *P* to *P* single scattering accounts for only a very small fraction of coda energy, probably less than 5%. Shallow *P* to *P* and *P* to *S* scattering, *P* to *Rg* scattering near the free surface, and multiple scattering comprise most of the *P*-wave coda.
20. I thank E. Humphreys and an anonymous reviewer for helpful comments and suggestions. This research was supported by the National Science Foundation. Lunchtime Software Guild contribution 13.

18 January 1995; accepted 11 April 1995

Structure and Density of FeS at High Pressure and High Temperature and the Internal Structure of Mars

Yingwei Fei, Charles T. Prewitt, Ho-kwang Mao, Constance M. Bertka

In situ x-ray diffraction measurements revealed that FeS, a possible core material for the terrestrial planets, transforms to a hexagonal NiAs superstructure with axial ratio (*c/a*) close to the ideal close-packing value of 1.63 at high pressure and high temperature. The high-pressure-temperature phase has shorter Fe-Fe distances than the low-pressure phase. Significant shortening of the Fe-Fe distance would lead to metallization of FeS, resulting in fundamental changes in physical properties of FeS at high pressure and temperature. Calculations using the density of the high-pressure-temperature FeS phase indicate that the martian core-mantle boundary occurs within the silicate perovskite stability field.

Iron sulfide (FeS) has been found in many meteorites and is believed to be a possible component of the cores of terrestrial planets such as Earth and Mars. Models of internal structure of the planets with sulfur-bearing cores require accurate determinations of phase relations and densities of FeS at high pressure and high temperature, but study has been difficult because it has not proven possible to quench the high-pressure-temperature phases. Previously, phase transitions in FeS have been investigated only at high pressure and room temperature (*1–5*) and at high temperature and ambient pressure (*6, 7*). We have developed techniques for determining the structure and density of materials under simultaneous high pressure and temperature conditions (*8*). In this study, we report the structure and density of FeS at high pressure and high temperature. We then use these data to evaluate the relation between the depth of the martian core-mantle boundary and the sulfur content of the core.

Stoichiometric FeS at ambient conditions, called troilite (FeS I), has a NiAs-type hexagonal structure with a ($\sqrt{3}a$, $2c$) unit cell. Troilite transforms to a MnP-type structure (FeS II) at 3.4 GPa (*5*). A high-pressure phase (FeS III) forms at pressures above 6.7 GPa (*1, 3*), although its structure is uncertain (*9*). We conducted in situ synchrotron x-ray diffraction measurements on FeS using an externally heated diamond-anvil cell with the sample loaded in a hydrostatic Ne pressure medium (*10*). At 300 K, we confirmed the two previously observed phase transitions. Upon heating the FeS sample at high pressures (>6.7 GPa), we observed a different x-ray diffraction pattern (Fig. 1). The diffraction pattern is much simpler than that of the high-pressure phase (FeS III) and can be indexed on a hexagonal cell. The calculated x-ray diffraction pattern, based on a NiAs-type hexagonal structure with a ($2a$, c) unit cell, agrees well with the observed data (Table 1). The experimental data demonstrate that this high-pressure-temperature phase, which we named FeS IV, has a NiAs-type superstructure lattice, in which the hexagonal layers of Fe and S are alternately stacked along the *c* axis and the Fe atoms are slightly displaced such that a perfectly repeating unit cell occurs by doubling the *a* distance. The axial ratio (*c/a*) of FeS IV is close to an ideal close-packing value of 1.63. The phase boundary of the FeS III–FeS IV transition (Fig. 2) was determined to be $P = -11.25 + 0.0485T$ (for pressure P in gigapascals and temperature T in kelvin). By analyzing the x-ray diffraction data, we also obtained the density of FeS IV as a function of pressure at high temperatures (Fig. 3A).

A high-temperature phase of FeS has also been observed at about 420 K and ambient pressure (*6, 7*). The structure of this high-temperature phase has been controversial (*5, 7*) because of a discrepancy resulting from the assumption that the high-temperature phase has the same structure as the intermediate high-pressure phase (FeS II). Our experimental data show that the high-temperature phase has a hexagonal structure with a ($2a$, c) unit cell, as reported by Keller-Besrest and Collin (*7*), and that the structure of the intermediate high-pressure phase (FeS II) is consistent with the MnP-type structure reported by King and Prewitt (*5*). The high-tempera-

Geophysical Laboratory and Center for High Pressure Research, Carnegie Institution of Washington, 5251 Broad Branch Road, NW, Washington, DC 20015, USA.